Environmental Science and Ecotechnology 29 (2026) 100652

Contents lists available at ScienceDirect

Environmental Science and Ecotechnology

journal homepage: www.journals.elsevier.com/environmental-science-and-ecotechnology/

Original Research

Ultrahigh-resolution 3D monitoring reveals sediment-derived plumes as algal bloom precursors

Peng Xiao [a,1], Congchao Zhang [a,1], Yu Tao [b,*], Tiefu Xu [c], Ying Chen [b], Lian Feng [d], Lingchao Kong [e,f], Zhidan Wen [g], Weibin Zheng [b], Hao Xu [b], Longxin Guo [b], Hangyu Guo [h], Zheng Pang [i], Zhiling Li [a], Chuan He [b], Shujie Xu [e,j], Kaishan Song [g], Jie Feng [k], Zhugen Yang [l], Shu-Chien Hsu [j], Chunmiao Zheng [f], Aijie Wang [a,b,**], Dragan Savic [m,n], Nanqi Ren [a,b]

[a] State Key Laboratory of Urban-Rural Water Resource and Environment, School of Environment, Harbin Institute of Technology, Harbin, 150086, China
[b] School of Eco-Environment, Harbin Institute of Technology, Shenzhen, 518055, China
[c] School of Civil Engineering, Heilongjiang University, Harbin, 150080, China
[d] State Key Laboratory of Information Engineering in Surveying, Mapping and Remote Sensing, Wuhan University, Wuhan, 430079, China
[e] School of Environmental Science and Engineering, Southern University of Science and Technology, Shenzhen, 518055, China
[f] School of the Environment and Sustainable Engineering, Eastern Institute of Technology, Ningbo, 315200, China
[g] Northeast Institute of Geography and Agroecology, Chinese Academy of Sciences, Changchun, 130102, China
[h] School of Environmental Science and Engineering, Nanjing Technology University, Nanjing, 211816, China
[i] Key Laboratory of Environmental Biotechnology, Research Center for Eco-Environmental Sciences, Chinese Academy of Sciences, Beijing, 100085, China
[j] Department of Civil and Environmental Engineering, The Hong Kong Polytechnic University, Hong Kong, China
[k] Shenzhen Academy of Environmental Sciences, Shenzhen, 518001, China
[l] Faculty of Engineering and Applied Sciences, Cranfield University, Cranfield, MK43 0AL, UK
[m] KWR Water Research Institute, Nieuwegein, 3430 BB, the Netherlands
[n] Centre for Water Systems, University of Exeter, Exeter, EX4 4QF, UK

ARTICLE INFO

Article history:
Received 23 May 2025
Received in revised form
25 December 2025
Accepted 25 December 2025

Keywords:
Harmful algal blooms (HABs)
Sediment-derived plumes
Ultrahigh-resolution
Three-dimensional (3D) monitoring
Early warning

ABSTRACT

The global intensification of harmful algal blooms severely compromises freshwater ecosystems, threatening biodiversity and critical ecosystem services through toxin exposure, hypoxia, and water quality degradation. Bloom formation involves a complex interplay of nutrient dynamics, hydrology, and microbial activity. Although subsurface processes—such as the release of sediment-bound nutrients and the germination of dormant cyanobacteria—are thought crucial to bloom initiation, these phenomena occur at fine spatiotemporal scales beyond the reach of conventional monitoring. As a result, the exact, rapidly evolving triggers of bloom emergence remain mostly unknown. Here we show meter-scale chlorophyll *a* (Chl-*a*) plumes rising from the sediment–water interface, triggered by heavy rainfall and directly seeding surface blooms. We captured these dynamics using a custom underwater drone that collected over 2.8 million data points at 5-m horizontal and 1-m vertical resolution. Algal blooms exhibit a clear vertical sequence: anomalous Chl-*a* levels first appear in deep benthic layers after rainfall-driven resuspension, then intensify simultaneously across near-bed depths, and finally reach the surface after a median lag of 0.8–1.5 days. These observations provide *in situ* evidence associating benthic algal seed stocks with surface bloom initiation, revealing that the origin and spatial heterogeneity of such events arise from rainfall-driven disturbances at the sediment–water interface. This robotic approach not only deciphers the subsurface origins of algal blooms but also empowers predictive modeling and adaptive management strategies, advancing global efforts to combat eutrophication amid escalating climate pressures and safeguard vital water resources.

© 2025 The Authors. Published by Elsevier B.V. on behalf of Chinese Society for Environmental Sciences, Harbin Institute of Technology, Chinese Research Academy of Environmental Sciences. This is an open access article under the CC BY-NC-ND license (http://creativecommons.org/licenses/by-nc-nd/4.0/).

* Corresponding author.
** Corresponding author. State Key Laboratory of Urban-Rural Water Resource and Environment, School of Environment, Harbin Institute of Technology, Harbin 150086, China.
E-mail addresses: taoyu@hit.edu.cn (Y. Tao), waj0578@hit.edu.cn (A. Wang).
[1] These authors contributed equally to this work.

https://doi.org/10.1016/j.ese.2025.100652
2666-4984/© 2025 The Authors. Published by Elsevier B.V. on behalf of Chinese Society for Environmental Sciences, Harbin Institute of Technology, Chinese Research Academy of Environmental Sciences. This is an open access article under the CC BY-NC-ND license (http://creativecommons.org/licenses/by-nc-nd/4.0/).

1. Introduction

The global intensification of harmful algal blooms (HABs) over the past four decades has emerged as a critical threat to aquatic biodiversity [1], public health [2], and water resource security [3]. This escalating prevalence necessitates urgent management interventions [4]; however, predicting and preventing HABs remains challenging due to complex interactions among nutrient availability [5], hydrodynamic conditions [6], and microbial physiology [7]. While the synergistic effects of external nutrient loading and climate warming are well documented [8–10], the physical–biological mechanisms that trigger bloom emergence—particularly the dynamics at the sediment–water interface—remain poorly resolved due to observational limitations, making precise quantification and forecasting difficult [6,11,12].

Emerging evidence increasingly points to the sediment–water interface as the critical initiation zone for bloom development [13–15]. Sediments serve as dual reservoirs, acting as both nutrient pools and seed banks capable of algal reactivation [16]. Physical disturbances, such as wind-induced mixing or rainfall-driven runoff, act as catalysts, resuspending these benthic stocks into the water column [15]. Concurrent thermal stratification can further accelerate nutrient release by inducing near-bed anoxia, creating favorable conditions for cyanobacterial recruitment [17,18]. Consequently, the vertical migration of biomass and nutrients from the benthos to the surface is hypothesized to be a primary precursor to surface blooms [9,19,20].

Despite the theoretical recognition of these benthic–pelagic coupling processes, *in situ* observation of sediment-derived precursors remains severely constrained by the resolution of conventional monitoring technologies [21,22]. A fundamental trade-off currently exists between spatial coverage and temporal frequency. Satellite remote sensing provides basin-scale coverage but is limited to the first optical depth, leaving subsurface dynamics obscured [18,19]. Similarly, traditional ship-based discrete sampling, while offering vertical resolution, has low temporal frequency and high labor costs, often missing transient vertical exchanges due to spatiotemporal aliasing [20]. Conversely, profiling buoys and fixed-point sensors offer high temporal resolution but are spatially confined to one-dimensional (i.e., vertical) transects, failing to capture the horizontal heterogeneity of patchy bloom initiation [23,24]. Even autonomous mobile platforms, such as gliders or cruising autonomous underwater vehicles, typically employ broad sawtooth trajectories that lack the sampling density required to resolve meter-scale vertical plumes [25]. We need to link benthic disturbances to surface proliferation to capture the exact triggers of bloom emergence.

In this study, we developed a meter-scale, 3D, daily monitoring framework capable of resolving water-quality dynamics. We equipped a remotely operated vehicle (ROV) with a multiparameter sonde and acquired over 2.8 million water-quality data points for 124 days. Applying these data, we captured repeated spatiotemporal evolution of sediment-derived Chl-*a* plumes. This study provides direct *in situ* evidence of the benthic-to-surface cascade, demonstrating how rainfall-driven disturbances at the sediment–water interface generate coherent plumes that seed surface blooms. These findings not only elucidate the subsurface origins of HABs but also demonstrate that ultrahigh-resolution 3D monitoring can detect bloom precursors days in advance of surface manifestation, offering a new paradigm for predictive modeling and early warning systems.

2. Materials and methods

2.1. Study area

The study was conducted in the tail zone of a reservoir located in Shenzhen, China (Fig. 1). This region covers approximately 6 ha of water surface area, with a total storage capacity of 3.66 million cubic meters. The reservoir is mainly supplied by a single tributary with a catchment area of 6.70 km^2, and outflow is controlled through dam gates. Routine background monitoring indicated generally low nutrient concentrations prior to the study period (details in Supplementary Method Section 4.1 and Supplementary Table S1).

2.2. Design and construction of the underwater drone

To resolve fine-scale spatiotemporal dynamics in stratified inland waters, we engineered a custom underwater drone that integrates continuous multiparameter sensing with discrete sample collection capabilities (Fig. 2a). The drone was built upon an ROV platform (Model W6, QYSEA Co., Ltd., China), designed for a maximum operational depth of 350 m. The ROV was equipped with a multiparameter water-quality sonde (Supplementary Table S2; EXO2, YSI, USA) that measures Chl-*a*, pH, dissolved oxygen (DO), conductivity, turbidity, fluorescent dissolved organic matter (FDOM), and temperature in real time. An array of eight 100-mL piston-actuated volumetric samplers is equipped to the ROV to collect both water and sediment samples. For sediment sampling, the drone was maneuvered vertically to penetrate the sediment–water interface and capture water-sediment mixtures (Fig. 2b). An ultra-short baseline acoustic positioning unit was equipped (Supplementary Fig. S1; UQPS-R300; QYSEA Co., Ltd., China; positioning accuracy: ±2 m horizontal, ±0.5 m vertical), achieving 1-m accuracy by triangulating signals between a shore-based global positioning system (GPS) unit, a shallow-water receiver, and the vehicle-mounted acoustic transmitter (details in Supplementary Method Section 1).

2.3. 3D grid design

A terrain-following grid is applied to enable systematic volumetric monitoring. The resolution of this grid is strictly determined by a physical constraint: the hydrodynamic disturbance generated by the drone itself. Since the drone operates using six propellers, it inevitably creates turbulence in the water. If this disturbance footprint overlaps with subsequent sampling points, it would mix the water column, leading to distorted data and measurement artifacts. To prevent such interference, it is essential to precisely know the spatial extent of the propeller-induced turbulence. Computational fluid dynamics (CFD) simulation reveals that forward propulsion generates the maximum disturbance, with a scale extending 4.05 m horizontally and 0.3 m vertically (details in Supplementary Method Section 2.3, Supplementary Fig. S2–S4 and Supplementary Table S3–S4). Consequently, by incorporating safety margins into these worst-case dimensions, we establish a grid resolution of 5 m horizontally and 1 m vertically to guarantee that each measurement is collected from undisturbed water.

Bathymetry was mapped using a multibeam sonar (Model BV5000-2250, Teledyne BlueView, Inc., USA) and interpolated via kriging (ArcGIS Pro) to generate a continuous terrain model (Supplementary Fig. S5). We projected a 5-m horizontal lattice

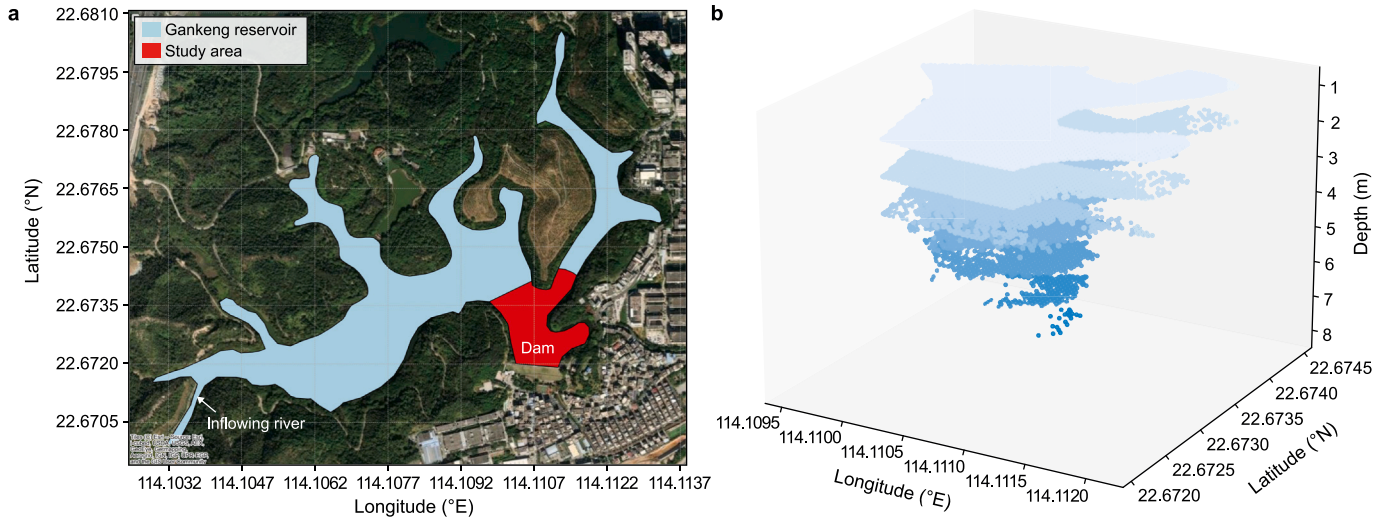

Fig. 1. Study area and ultrahigh-resolution 3D grid. a, Overview of the reservoir and surrounding catchment. The water body is highlighted in blue; red arrows indicate the locations of the inflowing river and the tail spillway dam. The red shaded area delineates the tail zone, the primary focus of monitoring activities. **b,** Ultrahigh-resolution 3D grid, comprising 8125 cells with 5-m horizontal and 1-m vertical resolution.

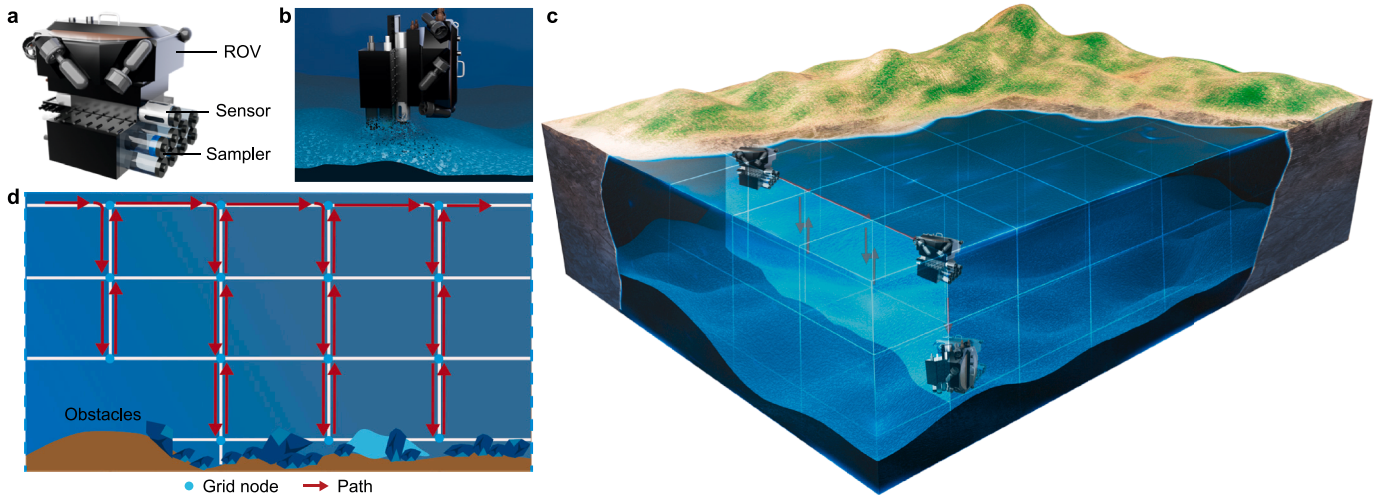

Fig. 2. Autonomous ultrahigh-resolution 3D monitoring framework. a, Platform architecture. The sensor suite and sampling array are integrated beneath the remotely operated vehicle (ROV) platform. **b,** Sediment sampling configuration. The drone adjusted its vertical orientation to penetrate the sediment–water interface for mixed sediment–water collection. **c,** 3D grid monitoring operation. The underwater drone navigated a predefined path through the cell, collecting data and samples exclusively at designated cells. **d,** Mission planning strategy. The drone used surface-based transit protocol for cell traversal, with all horizontal transit at the water surface to avoid benthic obstacles.

onto the water surface, defined as cells. From each surface cell, depth-specific coordinates are extruded vertically at 1-m intervals down to the benthic boundary (1–8 m), ensuring the grid conforms to the actual reservoir topography (Fig. 2c). In total, the study area has 8125 grid cells.

2.4. Trajectory design and operational protocol

Guided by preliminary field trials, we favor surface over subsurface cruising in our trajectory design, as surface horizontal motion offers two key advantages. First, surface operation enhances safety by enabling vision-based obstacle detection and avoidance. Second, regarding spatial fidelity, surface-based positioning is more accurate than underwater acoustic positioning, which is affected by signal attenuation and multipath errors. For these reasons, we adopted a strict surface-transit protocol—the drone performed all horizontal travel exclusively at the water surface (demonstrated in Video S1). Upon reaching a target cell, the vehicle descended to collect data at 1-m intervals (Fig. 2d). At each depth, the drone hovered to ensure data quality, with sensors updating at 5 Hz; a measurement was automatically recorded only after the Chl-*a* reading (resolved to two decimal places) remained identical for three periods. In practice, satisfying this strict criterion typically requires approximately 3 s per cell.

Supplementary video related to this article can be found at https://doi.org/10.1016/j.ese.2025.100652

At every cell, the underwater drone records a timestamp, geographic coordinates, and seven water quality parameters, all being logged in real time as CSV files. We conducted three rounds of water-quality monitoring daily throughout the 124-day experiment, except on Days 20–23, Day 34, Day 55, and Day 68, due to drone maintenance (see Videos S2–S8 for spatiotemporal

dynamics of all monitored parameters).

Supplementary video related to this article can be found at https://doi.org/10.1016/j.ese.2025.100652

2.5. Sensor validation

Sensor readings are cross-validated against laboratory spectrophotometric analysis to verify the accuracy of *in situ* fluorescence data. We collected 224 discrete water samples across depths of 1–8 m, paired with concurrent sensor measurements of Chl-*a*. Laboratory Chl-*a* concentrations were quantified via acetone extraction following United States Environmental Protection Agency Method 446.0 [26].

The statistical percentage difference agreement between the paired sensor and laboratory measurements was quantified using Bland–Altman analysis. For each data pair, the percentage difference was calculated as the difference between the sensor reading and the laboratory measurement, divided by the arithmetic mean of the two values. Depth-stratified validation confirmed stable, accurate Chl-*a* measurements throughout the water column, with high precision in the concentration range critical for bloom detection (Supplementary Fig. S6). In the assessment of bias and precision, 84.7% of measurements agreed with laboratory values within the practical acceptance limits of ±10% (grey lines), with the statistical limits of agreement shown as a light grey band. Theil–Sen regression revealed no systematic bias (the slope was not significantly different from zero). Although minor discrepancies were observed at low concentrations of 2–5 μg L^{-1}, the strongest agreement occurred at bloom-typical levels, particularly in the surface layer where Chl-*a* concentrations were highest.

2.6. Data analysis

Given the natural vertical stratification of light and biomass, we implement a depth-specific statistical framework—termed anomaly detection analysis—to systematically isolate Chl-*a* hotspots. By calculating the spatial mean (μ) and standard deviation (σ) independently for each depth layer, we establish dynamic thresholds ($\mu + 2\sigma$) specific to each monitoring horizon. This strategy successfully isolated spatiotemporal hotspots (i.e., anomalies), ensuring that systematic vertical gradients in baseline concentrations did not confound anomaly detection.

To quantify the spatial clustering of these anomalies, we compute a dispersion metric for each monitoring cycle. For all anomalies identified at a given time step, we define the spatial centroid using the mean longitude and latitude coordinates. The metric was then calculated as the arithmetic mean of the standard deviations of anomaly positions in both directions. Low metric values signify concentrated, localized plume structures, whereas high values indicate spatially scattered anomalies. This quantification enables precise tracking of plume coherence during both vertical ascent and subsequent horizontal expansion.

3. Results and discussion

3.1. Vertical propagation of rainfall-induced Chl-a anomalies from bed to surface

Continuous monitoring throughout the 124-day experiment captured the reservoir's dynamic response to meteorological forcing, with a particular focus on five heavy rainfall episodes. While Chl-*a* concentrations remained stable during quiescent intervals, precipitation events consistently perturbed the water column, triggering significant fluctuations in biomass. A systematic analysis of the 2.8 million data points revealed that these fluctuations did not co-occur across depths. Instead, the data uncovered a distinct three-stage phenomenological sequence: heavy-rainfall events first trigger near-bed Chl-*a* pulses, which subsequently ascend through the water column, and finally culminate in surface blooms.

Specific observations of five discrete heavy rainfall events (daily precipitation >25 mm) highlighted this coupling (Fig. 3). In the surface layer (1 m), Chl-*a* concentrations remained relatively steady (5–10 μg L^{-1}) during dry periods but surged rapidly following precipitation. For instance, a cumulative rainfall of 94.2 mm during Days 16–18 drove surface Chl-*a* from 5.2 to 19.2 μg L^{-1}, while a 47.3 mm event on Day 75 triggered a similar increase from 8.3 to 21.2 μg L^{-1}. Following each event, concentrations returned to baseline levels within 3–7 days, establishing a cyclical pattern of disturbance-driven amplification and subsequent decay.

Surface responses were systematically preceded by subsurface precursors, following a distinct vertical trajectory where elevated signals first emerged at 8 m, propagated upward to 5 m, and finally reached 1 m. Across the observed events, Chl-*a* peaks at 8 m exhibited a lead time of approximately 2 days relative to surface maxima, while Chl-*a* at 5 m led surface peaks by approximately 1 day. This vertical progression establishes Chl-*a* dynamics at 5 and 8 m as quantifiable precursors to surface blooms, confirming that the observed biomass accumulation initiates at the bottom rather than the surface.

This bottom-up trajectory was further corroborated by the vertical stratification of Chl-*a* variability. By pooling observations over the entire experiment, we calculated depth-specific standard deviations to quantify temporal stability. The analysis revealed a bimodal depth pattern: high variability was observed at 1 m (0.97 μg L^{-1}) and 8 m (2.0 μg L^{-1}), whereas intermediate depths (4 and 5 m) exhibited fivefold lower variability (0.32 and 0.38 μg L^{-1}). The surface peak reflects rapid algal growth and photoaccumulation, while the pronounced near-bed peak is consistent with episodic sediment disturbances. These disturbances may cause discrete pulses of benthic algal biomass, generating intermittent near-bed maxima that are distinct from surface dynamics.

3.2. Coherent vertical ascent of sediment-derived plumes seeds surface blooms

While Section 3.1 established the temporal lag between bottom and surface signals, determining the physical mechanism of this transport requires resolving the 3D structure of the rising water mass. To achieve this, we analyzed ultrahigh-resolution observations during a representative heavy rainfall event (Days 59–62, 23.2 mm hr^{-1} starting at 13:00). Unlike point measurements, this dataset—comprising 12 consecutive drone surveys over four days—captured the complete spatial evolution of the bloom, allowing us to reconstruct the mechanistic cascade connecting sediment disturbance to surface proliferation. Based on this dataset, we used the depth-specific statistical framework to systematically isolate Chl-a hotspots (Fig. 4a).

A rainfall event triggered a rapid inversion of the vertical Chl-*a* profile (Fig. 4b). Prior to the event (09:00 on Day 59), Chl-*a* concentrations were elevated in the surface layer (8.0–10.2 μg L^{-1}), while those of 2–8 m remained below 3.0 μg L^{-1}. However, immediately following the rainfall onset (13:00), this structure was upended. Surface concentrations dropped to 6.5 μg L^{-1} due to dilution by rainwater inflow, whereas near-bed concentrations (7–8 m) surged to over 9.0 μg L^{-1}. This threefold increase in deep-water biomass marked the initiation of the disturbance event.

To determine whether this deep-water surge resulted from density-driven lateral intrusion or local sediment resuspension,

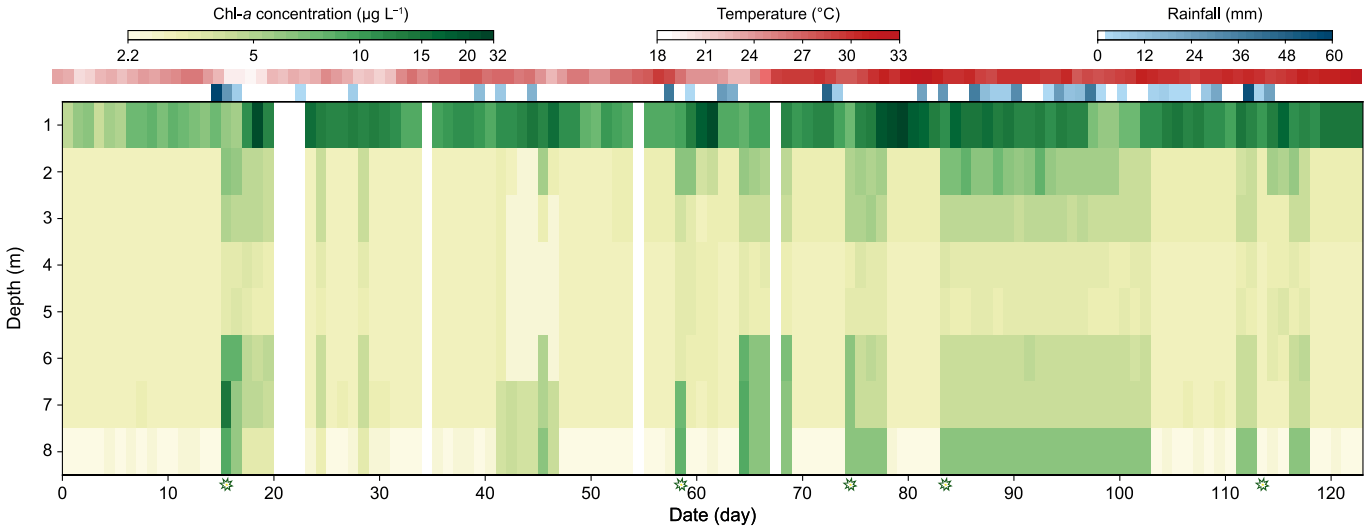

Fig. 3. High-resolution spatiotemporal evolution of Chl-*a* concentrations (9 Mar–10 Jul 2023). The depth–time heatmap visualizes daily mean Chl-*a* concentrations across the 1–8 m water column, derived from ultrahigh-resolution 3D monitoring (drone surveys: 5 m × 1 m grid, three daily volumetric surveys). Top ribbons display concurrent meteorological conditions: surface temperature (red) and rainfall (blue). White gaps in the heatmap indicate periods of missing data, while green asterisks mark identified bloom events. The data reveal complex vertical stratification and transient biomass dynamics often obscured in conventional datasets.

we analyzed conductivity profiles, one of the seven parameters measured by the sensors. The observed conductivity difference between surface and bottom corresponded to a negligible density contrast ($\Delta\rho = 0.003$ kg m^{-3}), which is an order of magnitude below the threshold required to sustain gravity-current intrusions in stratified systems (0.05 kg m^{-3}). The absence of a sufficient density gradient, combined with the synchronous Chl-*a* surge across the 2–8 m layer, confirmed that the primary driver was not external intrusion, but rather rainfall-generated turbulence resuspending Chl-*a*-rich sediment and dormant algal cells.

Following resuspension, the spatial distribution of Chl-*a* evolved through distinct phases (Fig. 4c). We tracked three-dimensional Chl-*a* anomalies and quantified their spatial clustering over time. At 13:00 on Day 59, the spatial dispersion metric was 6.789×10^{-4}, reflecting scattered Chl-*a* anomalies resulting from surface disruption. By 17:00 on Day 59, this metric had decreased by 42%. This convergence reflected the formation of discrete, vertically coherent plumes spanning from 8 to 1m, indicating rapid upward transport. The low dispersion value during this phase confirms that anomalies were spatially concentrated, consistent with organized vertical ascent. On Day 60, the dispersion metric increased by 69% to 6.668×10^{-4}, marking the completion of vertical transport and the initiation of lateral dispersion. Localized maxima in the northwestern sector reached 15.3 μg L^{-1}. By Day 62, dispersion peaked at 7.237×10^{-4}. This reservoir-wide dispersion directly drove the rapid intensification of the surface bloom: as the plume expanded, it fueled a 176% surge in Chl-*a* hotspot intensity (reaching 42.4 μg L^{-1}) and substantiated a 71.6% increase in the reservoir-wide mean surface Chl-*a* concentration.

These observations demonstrate that sediment-derived plumes do not disperse immediately upon release; instead, they ascend as coherent structures. This structural integrity is critical for transport efficiency, as it prevents dilution during the ascent. The temporal trajectory of spatial dispersion—convergence during vertical lift followed by divergence during horizontal spread—confirms that benthic disturbances directly seed surface blooms by injecting sediment-associated algae into photic zones.

3.3. Benthic-pelagic coupling: Co-regulation of surface bloom geography by sediment stocks and physical forcing

Surface Chl-*a* concentrations exhibited persistent spatial heterogeneity, with high-biomass hotspots consistently recurring in specific regions (Fig. 5a). We test the hypothesis that this surface patterning mirrors the distribution of benthic algal stocks. A comparison across 90 sites over the 124 days revealed a robust correlation between surface Chl-*a* and the near-bed nepheloid-layer Chl-*a* proxy (NBNLC, $R^2 = 0.73, n = 90, p = 0.006$; Fig. 5b, details in Supplementary Method Section 3.3 and Supplementary Fig. S7–S8). This strong spatial concordance indicates that the geography of surface blooms is not random but is structurally anchored to benthic source regions. Sediment thus functions as spatially variable recruitment sources, pre-determining the specific locations where biomass accumulates.

We identified two environmental drivers that govern this benthic-pelagic coupling through distinct mechanistic roles: light availability as a basin-wide enabler, and physical forcing as a localized trigger.

First, photosynthetically active radiation above the sediment (BottomPAR; details in Supplementary Method Section 4.3) acted as the metabolic prerequisite. BottomPAR exceeded 1.1 W m^{-2} ($\approx$ 0.24 mol photons m^{-2} d^{-1}) at the majority of sites (Fig. 5c), surpassing the physiological threshold for benthic microalgal activity. This widespread light availability enabled benthic algae to maintain viability across the reservoir bed, establishing a basin-wide potential for bloom initiation. Consequently, correlations between BottomPAR and surface Chl-*a* were spatially extensive and stronger than for other variables (Fig. 5d), confirming that light modulates the baseline magnitude of the algal stock available for resuspension.

Second, the compound wind–precipitation strength (CWP; details in Supplementary Method Section 4.2 and Supplementary Fig. S9) acted as the spatially selective trigger. Unlike the uniform distribution of light, CWP exhibited strong gradients, peaking in the wind-exposed northern reach where shear stress exceeded critical mobilization thresholds and diminishing in the sheltered

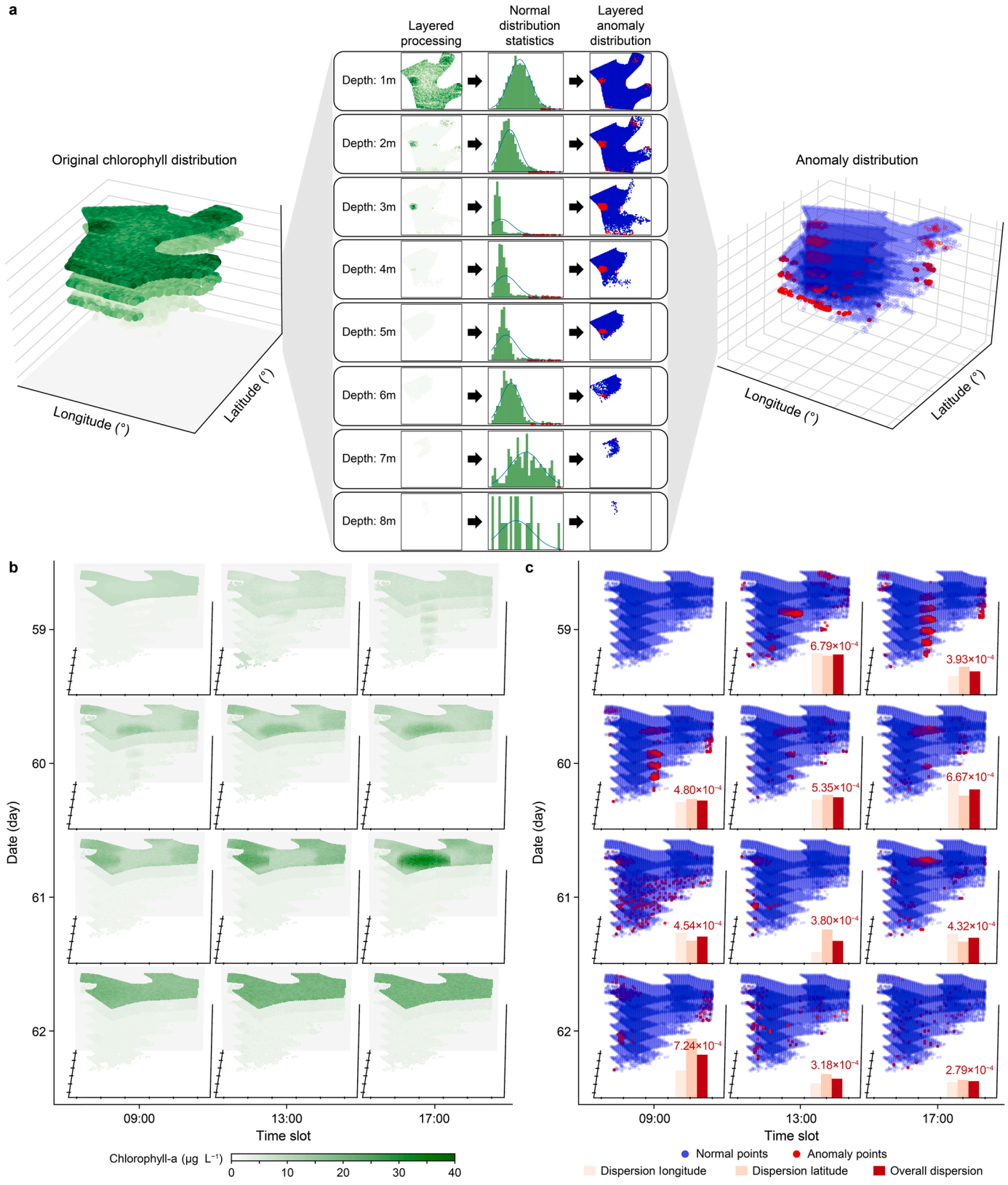

Fig. 4. 3D reconstruction of Chl-*a* dynamics and anomaly detection. a, Data processing workflow. Left panel: Raw 3D Chl-*a* concentration distribution. Central panel: Depth-stratified statistical analysis (1–8 m at 1-m intervals). Baselines were established assuming a normal distribution, and concentrations exceeding twice the standard deviation ($\mu + 2\sigma$) were identified as anomalies. Right panel: Reconstructed 3D distribution of water quality anomalies. **b,** High-resolution spatiotemporal evolution of Chl-*a* during the bloom event (Days 59–62). Panels depict the instantaneous 3D Chl-*a* structure derived from 8125 measurement points per cruise. Note the occurrence of heavy rainfall (23.2 mm h^{-1}) starting at 13:00 on Day 59. **c,** 3D visualization of local anomalies. Post-rainfall visualizations reveal vertically expanding sediment-derived plumes that spatially converge toward surface bloom zones, indicating their role as precursors. Centroid dispersion metrics (longitudinal, latitudinal, and overall) quantifying spatial coherence are displayed above the corresponding time–depth layers.

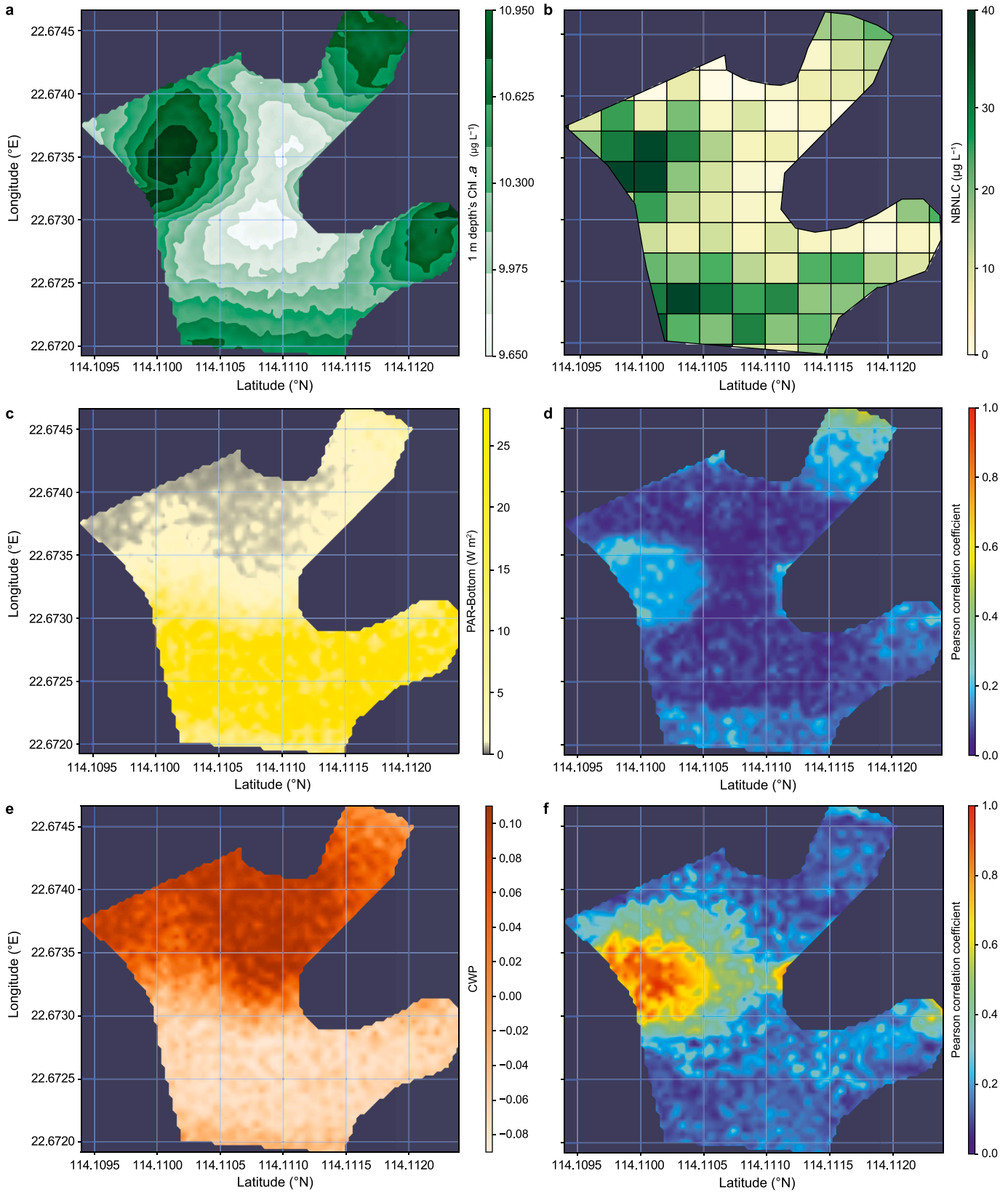

Fig. 5. Spatial coupling between surface Chl-*a* and benthic drivers (Temporal means, Days 11;124). a, Mean near-surface Chl-*a* distribution (1 m depth; μg L^{-1}). **b,** Near-bed nepheloid-layer Chl-*a* proxy (NBNLC; μg L^{-1}). Data are mapped onto a fixed 90-cell; colors represent site-specific means (n = 90). NBNLC serves as a water-phase proxy for pigment resuspension in the nepheloid layer (details in Supplementary Method Section 3.3). **c,** Compound wind–precipitation strength (CWP; dimensionless z-score). Values represent the integrated impulse of rainfall–runoff and wind shear exceeding depth- and fetch-dependent critical velocities (details in Supplementary Method Section 4.2). **d,** Bottom photosynthetically active radiation (BottomPAR; W m^{-2}) at the sediment–water interface, derived by scaling surface PAR with site-specific attenuation coefficients (details in Supplementary Method Section 4.3). **e–f,** Spatial distribution of Spearman's rank correlation coefficients (ρ) for 1 m Chl-*a* versus CWP (**e**) and BottomPAR (**f**) over the study period. BottomPAR explains variability across most sub-basins, whereas localized wind-exposed, sediment-rich sectors exhibit strong coupling with CWP (ρ up to ~0.77).

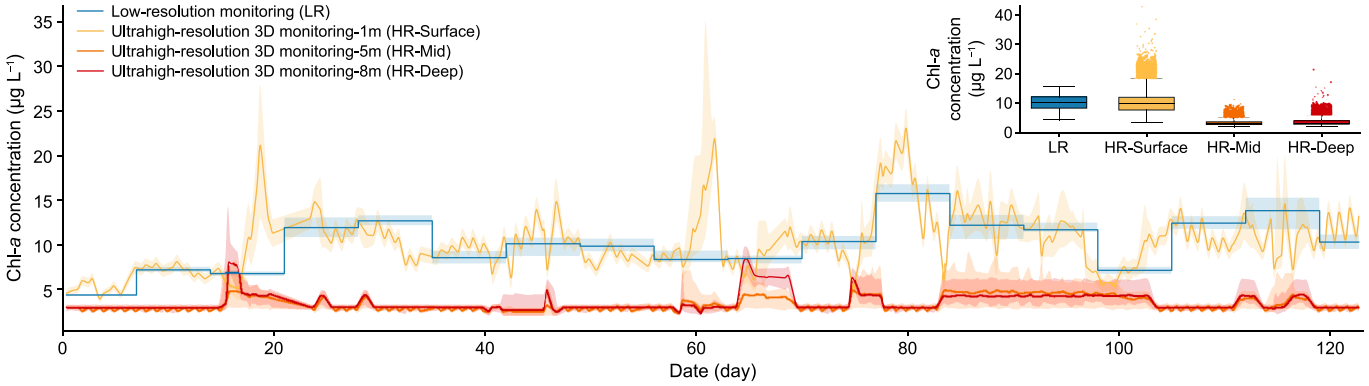

Fig. 6. Observational advantages of ultrahigh-resolution 3D monitoring over routine sampling. The analysis contrasts a low-resolution monitoring simulation (emulating routine manual sampling: 1 m depth, four sites, weekly) with the actual ultrahigh-resolution 3D monitoring dataset. Time-series comparison at 1, 5, and 8 m depths. Ultrahigh-resolution data are displayed as daily medians with 95% spatial confidence envelopes (shaded areas), whereas low-resolution data are shown as discrete weekly points. The ultrahigh-resolution approach resolves rapid pulses and vertical propagation that low-resolution monitoring fails to detect or capture with significant latency. Inserted panel: Comparative statistical distributions of Chl-*a* concentrations (Box: interquartile range [IQR]; Center line: median; Whiskers: 1.5 × IQR; Points: outliers). While central tendencies at the surface (1 m) appear similar between methods, the ultrahigh-resolution monitoring reveals significantly more extreme events (high-magnitude excursions) across all depth layers, highlighting the risk of underestimation by conventional protocols.

southern dam region (Fig. 5e). The relationship between CWP and surface Chl-*a* was not uniform but formed distinct hotspots. Peak correlations ($\rho = 0.77$) occurred specifically where high wind exposure coincided with dense benthic stocks (Fig. 5f). This pattern indicates that episodic wind-rain forcing amplifies blooms selectively, "unlocking" the benthic biomass only in regions where physical disturbance is sufficient to mobilize the sediment.

Collectively, these findings demonstrate a co-regulation mechanism shaping bloom geography. While BottomPAR primes the system by maintaining a widespread reservoir of benthic algae, CWP determines the timing and location of their release. The strong correlation between benthic proxies and surface Chl-*a* confirms that surface heterogeneity arises primarily from spatial variability in sediment sources and physical mobilization, rather than from differential growth rates within the water column alone.

3.4. Necessity of ultrahigh-resolution 3D monitoring

The detection of sediment-derived precursors is fundamentally constrained by monitoring resolution. To quantify the observational advantages of our approach, we compared the ultrahigh-resolution 3D monitoring against a simulated conventional low-resolution monitoring protocol.

We contrasted the two strategies by extracting parallel datasets from the campaign. The ultrahigh-resolution 3D approach surveyed the entire reservoir, yielding 8125 cells. In contrast, the simulated conventional protocol mimicked standard practice: weekly sampling at four fixed sites, restricted to the surface layer. To isolate the value of vertical resolution, we analyzed time series at three representative depths: surface (1 m), mid-layer (5 m), and near-bed (8 m). We selected 5 m as the mid-layer proxy due to its statistical representativeness of the 4–5 m depth interval (variance difference <3%, $r > 0.98$ across all cells).

The comparison revealed fundamental disparities in early warning capability (Fig. 6). The ultrahigh-resolution 3D monitoring successfully resolved short-lived Chl-*a* pulses lasting 2–4 days and captured their vertical progression. The median lead times were quantified at 1.5 days (from near-bed to surface). Conversely, conventional low-resolution sampling suffered from severe temporal aliasing. It failed to record the rapid dynamics, detecting only a fraction of the events with substantial delays. For instance, during the Day 59–62 event, the high-resolution data captured the full sequence—onset at 8 m (Day 59), intensification at 5 m (Day 60), and surface peak (Day 61). The conventional protocol, however, did not register the event until Day 63. Consequently, it missed the entire subsurface precursor phase and the critical initial bloom expansion.

Beyond timing, the two methods diverged significantly in quantifying risk magnitude. While both high-resolution and low-resolution monitoring yielded similar median Chl-*a* concentrations at 1 m (8.2 vs. 8.5 μg L^{-1}) and comparable interquartile ranges (5.8–12.1 vs. 6.1–11.8 μg L^{-1}; Fig. 6), the high-resolution monitoring captured significantly more extreme events, recording a 95th percentile of 18.7 μg L^{-1} compared to 15.2 μg L^{-1} for the low-resolution monitoring. The ultrahigh-resolution 3D monitoring revealed that Chl-*a* concentration medians at 5 and 8 m were lower (4.1 and 3.2 μg L^{-1}, respectively) yet exhibited intermittent high-magnitude excursions (95th percentiles: 11.3 and 9.8 μg L^{-1}). These results demonstrate that Chl-*a* maxima are highly transient. This systematic failure to resolve transient, subsurface dynamics confirms that conventional protocols are susceptible to severe spatiotemporal aliasing. Consequently, ultrahigh-resolution 3D monitoring represents an essential methodological advance required to elucidate the complex benthic-pelagic coupling driving reservoir bloom dynamics.

4. Concluding remarks

Ultrahigh-resolution monitoring offers a different perspective on the nature of algal bloom initiation. Conventional views often treat blooms as stochastic events driven by broad seasonal shifts; however, our findings substantiate a deterministic benthic-to-surface cascade driven by transient physical forcing. By resolving the spatiotemporal continuity of this process, we delineate a distinct three-stage mechanistic sequence: (1) benthic mobilization, where hydrodynamic disturbances resuspend nutrient-rich sediment and dormant cysts; (2) vertical transport, where basal plumes ascend as coherent structures over a 0.8–1.5 day period; and (3) surface proliferation, where recruited biomass initiates basin-scale expansion upon entering the photic zone. This capacity to record sub-weekly, stepwise dynamics provides the missing link in understanding how benthic legacies are reactivated to fuel pelagic eutrophication.

From a management perspective, these findings advocate for a

paradigm shift from reactive mitigation to preemptive, precision intervention. Surface water quality is mechanistically linked to precursors initiated days earlier at the sediment–water interface. This finding offers a critical early-warning window. Instead of relying on costly and ecologically intrusive whole-lake measures, management efforts should target specific seeding hotspots—regions identified by underwater drone surveys where high benthic stocks coincide with elevated hydrodynamic stress. Precision interventions, such as localized sediment capping or dredging in these high-risk zones, could suppress bloom formation at the source. As global climate pressures intensify, aquatic instability will increase, making high-resolution, process-based monitoring essential for safeguarding freshwater ecosystem resilience.

Notwithstanding these contributions, three key limitations warrant consideration in the future. First, regarding mechanistic verification, while we documented the physical ascent of Chl-*a* plumes, the subsequent physiological activation (germination) of these transported cells remains a black box in our current dataset; confirming viability will require future integration with high-frequency nutrient profiling and molecular analysis. Second, regarding technical scalability, expanding this framework to larger, morphologically complex lake systems remains challenging, necessitating advancements in long-endurance ROV. Finally, regarding ecological generalizability, it is important to note that our study was conducted in an oligotrophic reservoir. As such, the observed relationships between sediment disturbances and surface blooms may not directly translate to nutrient-rich lakes with different circulation patterns, where the coupling of these processes is likely more complex.

CRediT authorship contribution statement

Peng Xiao: Writing - Original Draft, Methodology, Conceptualization. **Congchao Zhang:** Investigation, Writing - Review & Editing. **Yu Tao:** Writing - Review & Editing, Funding Acquisition, Conceptualization, Supervision. **Tiefu Xu:** Writing - Review & Editing. **Ying Chen:** Writing - Review & Editing, Methodology, Formal Analysis. **Lian Feng:** Writing - Review & Editing. **Lingchao Kong:** Writing - Review & Editing. **Zhidan Wen:** Writing - Review & Editing, Formal Analysis. **Weibin Zheng:** Visualization, Formal Analysis. **Hao Xu:** Investigation, Writing - Review & Editing. **Longxin Guo:** Investigation, Writing - Review & Editing. **Hangyu Guo:** Investigation, Writing - Review & Editing. **Zheng Pang:** Investigation, Writing - Review & Editing. **Zhiling Li:** Writing - Review & Editing. **Chuan He:** Writing - Review & Editing, Visualization. **Shujie Xu:** Formal Analysis, Writing - Eeview & Editing. **Kaishan Song:** Writing - Review & Editing. **Jie Feng:** Writing - Review & Editing. **Zhugen Yang:** Writing - Review & Editing. **Shu-Chien Hsu:** Writing - Review & Editing. **Chunmiao Zheng:** Writing - Review & Editing. **Aijie Wang:** Writing - Review & Editing, Funding Acquisition, Supervision. **Dragan Savic:** Writing - Review & Editing. **Nanqi Ren:** Funding Acquisition, Supervision.

Declaration of competing interest

The authors declare that they have no known competing financial interests or personal relationships that could have appeared to influence the work reported in this paper.

Dr. Yu Tao, the Managing Editor of *Environmental Science and Ecotechnology*; Dr. Weibin Zheng and Miss Chuan He, the Editor of *Environmental Science and Ecotechnology*; Dr. Zhugen Yang, the Editorial Board Member of *Environmental Science and Ecotechnology*; Dr. Aijie Wang, the Executive Editor of *Environmental Science and Ecotechnology*; Dr. Dragan Savic, the Advisory Board Member of *Environmental Science and Ecotechnology*; and Dr. Nanqi Ren, the Editor-in-Chief of *Environmental Science and Ecotechnology*, were not involved in the editorial review or the decision to publish this article.

Acknowledgements

This work was supported by the National Natural Science Foundation of China (No. 52321005, No. 52293443, and No. 52230004), Shenzhen Science and Technology Program (No. KQTD20190929172630447), Shenzhen Key Research Project (No. GXWD20220817145054002), Shenzhen Natural Science Foundation (No. JCYJ20240813104812017), and Talent Recruitment Project of Guangdong (No. 2021QN020106).

Appendix A. Supplementary data

Supplementary data to this article can be found online at https://doi.org/10.1016/j.ese.2025.100652.

References

[1] M. Masó, E. Garcés, Harmful microalgae blooms (HAB); problematic and conditions that induce them, Mar. Pollut. Bull. 53 (2006) 620–630, https://doi.org/10.1016/j.marpolbul.2006.08.006.
[2] H.E. Plaas, H.W. Paerl, Toxic cyanobacteria: a growing threat to water and air quality, Environ. Sci. Technol. 55 (2021) 44–64, https://doi.org/10.1021/acs.est.0c06653.
[3] J. Merder, T. Harris, G. Zhao, D.M. Stasinopoulos, R.A. Rigby, A.M. Michalak, Geographic redistribution of microcystin hotspots in response to climate warming, Nat. Water 1 (2023) 844–854, https://doi.org/10.1038/s44221-023-00138-w.
[4] H.W. Paerl, W.S. Gardner, K.E. Havens, A.R. Joyner, M.J. McCarthy, S.E. Newell, B. Qin, J.T. Scott, Mitigating cyanobacterial harmful algal blooms in aquatic ecosystems impacted by climate change and anthropogenic nutrients, Harmful Algae 54 (2016) 213–222, https://doi.org/10.1016/j.hal.2015.09.009.
[5] Y. Tong, W. Zhang, X. Wang, R.-M. Couture, T. Larssen, Y. Zhao, J. Li, H. Liang, X. Liu, X. Bu, et al., Decline in Chinese lake phosphorus concentration accompanied by shift in sources since 2006, Nat. Geosci. 10 (2017) 507–511, https://doi.org/10.1038/ngeo2967.
[6] R.I. Woolway, S. Sharma, G.A. Weyhenmeyer, A. Debolskiy, M. Golub, D. Mercado-Bettín, M. Perroud, V. Stepanenko, Z. Tan, L. Grant, et al., Phenological shifts in lake stratification under climate change, Nat. Commun. 12 (2021), https://doi.org/10.1038/s41467-021-22657-4.
[7] D. Donis, E. Mantzouki, D.F. McGinnis, D. Vachon, I. Gallego, H.P. Grossart, L.N. de Senerpont Domis, S. Teurlincx, L. Seelen, M. Lürling, et al., Stratification strength and light climate explain variation in chlorophyll a at the continental scale in a European multilake survey in a heatwave summer, Limnol. Oceanogr. 66 (2021) 4314–4333, https://doi.org/10.1002/lno.11963.
[8] X.Z. Kong, M. Determann, T.K. Andersen, C.C. Barbosa, T. Dadi, A.B.G. Janssen, M.C. Paule-Mercado, D.G.F. Pujoni, M. Schultze, K. Rinke, Synergistic effects of warming and internal nutrient loading interfere with the long-term stability of Lake restoration and induce sudden Re-eutrophication, Environ. Sci. Technol. 57 (2023) 4003–4013, https://doi.org/10.1021/acs.est.2c07181.
[9] M.M. Kalcic, R.L. Muenich, S. Basile, A.L. Steiner, C. Kirchhoff, D. Scavia, Climate change and nutrient loading in the Western Lake Erie Basin: warming can counteract a wetter future, Environ. Sci. Technol. 53 (2019) 7543–7550, https://doi.org/10.1021/acs.est.9b01274.
[10] J.R. Seymour, S.L. Mclellan, Climate change will amplify the impacts of harmful microorganisms in aquatic ecosystems, Nat. Microbiol. 10 (2025) 615–626, https://doi.org/10.1038/s41564-025-01948-2.
[11] W.S. Gardner, S.E. Newell, M.J. McCarthy, D.K. Hoffman, K. Lu, P.J. Lavrentyev, F.L. Hellweger, S.W. Wilhelm, Z. Liu, D.A. Bruesewitz, H.W. Paerl, Community biological ammonium demand: a conceptual model for Cyanobacteria blooms in eutrophic Lakes, Environ. Sci. Technol. 51 (2017) 7785–7793, https://doi.org/10.1021/acs.est.6b06296.
[12] H.S. Anderson, T.H. Johengen, R. Miller, C.M. Godwin, Accelerated sediment phosphorus release in Lake Erie's central basin during seasonal anoxia, Limnol. Oceanogr. 66 (2021) 3582–3595, https://doi.org/10.1002/lno.11900.
[13] J. Huisman, G.A. Codd, H.W. Paerl, B.W. Ibelings, J.M.H. Verspagen, P.M. Visser, Cyanobacterial blooms, Nat. Rev. Microbiol. 16 (2018) 471–483, https://doi.org/10.1038/s41579-018-0040-1.
[14] Y. Du, S. An, H. He, S. Wen, P. Xing, H. Duan, Production and transformation of organic matter driven by algal blooms in a shallow lake: role of sediments, Water Res. 219 (2022) 118560, https://doi.org/10.1016/j.watres.2022.118560.
[15] W.-J. Cai, X. Hu, W.-J. Huang, M.C. Murrell, J.C. Lehrter, S.E. Lohrenz, W.-C. Chou, W. Zhai, J.T. Hollibaugh, Y. Wang, et al., Acidification of subsurface coastal waters enhanced by eutrophication, Nat. Geosci. 4 (2011) 766–770, https://doi.org/10.1038/ngeo1297.

[16] B.F. Zheng, A.J. Lucas, P.J.S. Franks, T.L. Schlosser, C.R. Anderson, U. Send, K. Davis, A.D. Barton, H.M. Sosik, Dinoflagellate vertical migration fuels an intense red tide, P Natl Acad Sci USA 120 (2023). ARTN e230459012010.1073/pnas.2304590120.
[17] A.P. Kirol, A.M. Morales-Williams, D.C. Braun, C.L. Marti, O.E. Pierson, K.J. Wagner, A.W. Schroth, Linking sediment and water column phosphorus dynamics to oxygen, temperature, and aeration in shallow eutrophic Lakes, Water Resour. Res. 60 (2024), https://doi.org/10.1029/2023wr034813.
[18] R.I. Woolway, Y. Tong, L. Feng, G. Zhao, D.A. Dinh, H. Shi, Y. Zhang, K. Shi, Multivariate extremes in lakes, Nat. Commun. 15 (2024), https://doi.org/10.1038/s41467-024-49012-7.
[19] L. Qi, C. Hu, P.M. Visser, R. Ma, Diurnal changes of Cyanobacteria blooms in Taihu Lake as derived from GOCI observations, Limnol. Oceanogr. 63 (2018) 1711–1726, https://doi.org/10.1002/lno.10802.
[20] F. Chai, K.S. Johnson, H. Claustre, X. Xing, Y. Wang, E. Boss, S. Riser, K. Fennel, O. Schofield, A. Sutton, Monitoring ocean biogeochemistry with autonomous platforms, Nat. Rev. Earth Environ. 1 (2020) 315–326, https://doi.org/10.1038/s43017-020-0053-y.
[21] M. Bieroza, S. Acharya, J. Benisch, R.N. ter Borg, L. Hallberg, C. Negri, A. Pruitt, M. Pucher, F. Saavedra, K. Staniszewska, et al., Advances in catchment science, hydrochemistry, and aquatic ecology enabled by high-frequency water quality measurements, Environ. Sci. Technol. 57 (2023) 4701–4719, https://doi.org/10.1021/acs.est.2c07798.
[22] E. Calamita, J.J. Lever, C. Albergel, R.I. Woolway, D. Odermatt, Detecting climate-related shifts in lakes: a review of the use of satellite Earth observation, Limnol. Oceanogr. 69 (2024) 723–741, https://doi.org/10.1002/lno.12498.
[23] T. Fujiki, R. Inoue, M.C. Honda, M. Wakita, Y. Mino, C. Sukigara, O. Abe, Time-series observations of photosynthetic oxygen production in the subtropical western North Pacific by an underwater profiling buoy system, Limnol. Oceanogr. 65 (2019) 1072–1084, https://doi.org/10.1002/lno.11372.
[24] J.R. Corman, J.A. Zwart, J. Klug, D.A. Bruesewitz, E. de Eyto, M. Klaus, L.B. Knoll, J.A. Rusak, M.J. Vanni, M.B. Alfonso, et al., Response of lake metabolism to catchment inputs inferred using high-frequency lake and stream data from across the northern hemisphere, Limnol. Oceanogr. 68 (2023) 2617–2631, https://doi.org/10.1002/lno.12449.
[25] Y. Zhang, J.P. Ryan, B.W. Hobson, B. Kieft, A system of coordinated autonomous robots for Lagrangian studies of microbes in the oceanic deep chlorophyll maximum, Sci. Robot. 8 (2021).
[26] E.J. Arar, G.B. Collins, Method 446.0 in Vitro Determination of Chlorophylls A, B, c1 + c2 and Pheopigments in Marine and Freshwater Algae by Visible Spectrophotometry, U.S. Environmental Protection Agency, Office of Research and Development, 1997. National Exposure Research Laboratory.